SAND2007-0912C

Microstructural modeling of ferroic switching and phase transitions in PZT

Joshua Robbins[a], Tariq A. Khraishi[b] and Pavel M. Chaplya[c]

[a]Multiscale Dynamic Material Modeling, Sandia National Laboratories
Albuquerque, NM 87123, USA
[b] Mechanical Engineering Department, University of New Mexico
Albuquerque, NM 87131, USA
[c]Applied Mechanics Development, Sandia National Laboratories
Albuquerque, NM 87123, USA

ABSTRACT

Niobium doped Lead Zirconate Titanate (PZT) with a Zr/Ti ratio of 95/5 (i.e., PZT 95/5-2Nb) is a ferroelectric with a rhombohedral structure at room temperature. A crystal (or a subdomain within a crystal) exhibits a spontaneous polarization in any one of eight crystallographically equivalent directions. Such a material becomes polarized when subjected to a large electric field. When the electric field is removed, a remanent polarization remains and a bound charge is stored. A displacive phase transition from a rhombohedral ferroelectric phase to an orthorhombic anti-ferroelectric phase can be induced with the application of a mechanical load. When this occurs, the material becomes depoled and the bound charge is released. The polycrystalline character of PZT 95/5-2Nb leads to highly non-uniform fields at the grain scale. These local fields lead to very complex material behavior during mechanical depoling that has important implications to device design and performance.

This paper presents a microstructurally based numerical model that describes the 3D non-linear behavior of ferroelectric ceramics. The model resolves the structure of polycrystals directly in the topology of the problem domain and uses the extended finite element method (X-FEM) to solve the governing equations of electromechanics. The material response is computed from anisotropic single crystal constants and the volume fractions of the various polarization variants (i.e., three variants for rhombohedral anti-ferroelectric and eight for rhomobohedral ferroelectric ceramic). Evolution of the variant volume fractions is governed by the minimization of internally stored energy and accounts for ferroelectric and ferroelastic domain switching and phase transitions in response to the applied loads. The developed model is used to examine hydrostatic depoling in PZT 95/5-2Nb.

1. INTRODUCTION

Solid solutions of Lead Zirconate and Lead Titanate, $Pb(Ti, Zr)O_3$ or PZT, have found widespread application owing to their very desirable piezoelectric properties.[1] Depending on the particular solution and the temperature, PZT exhibits three polar phases – rhombohedral, tetragonal, and orthorhombic. Niobium doped PZT with a Zr/Ti ratio of 95/5 (PZT 95/5-2Nb) has a rhombohedral structure at room temperature and has a spontaneous polarization in any one of eight crystallographically equivalent directions (body diagonals). At a hydrostatic pressure of about 250 MPa the material undergoes a displacive phase transition to an orthorhombic anti-ferroelectric state. This phase transition from a polar to an anti-polar phase makes PZT 95/5-2Nb an excellent candidate for mechanically actuated power supplies.[2]

Ferroceramics are polycrystalline in character and a typical grain has regions of uniform polarization, called *domains*, that are separated by *domain walls*. The crystallographic basis of each grain is randomly oriented which, in combination with anisotropic single crystal behavior, leads to large variations in internal stress and electric field. Pores and impurities lead to further variation in internal fields.

The technological importance of ferroceramics has lead to extensive research in this area. Great effort over the last several decades has been expended in developing detailed and accurate understanding of ferroceramics. Experimental studies[3–5] have produced excellent insight into the physical origins of ferroelectric response, and have further fueled development of models capable of explaining and reproducing observed material behavior.

A common approach to modeling ferroceramic materials or devices is to enforce the appropriate conservation laws and kinematic relationships using the finite element method (FEM). Using this approach, ferroelectric response can be explored for arbitrary sample/device configurations and applied loads/constraints. However, in order to apply the FEM, the conservation equations and kinematic relationships must be accompanied by a constitutive model to form a complete and solvable system of equations. Fairly recently, perhaps over the last decade, many models of varying levels of sophistication have been proposed that attempt to model ferroelectric response by directly modeling the microscopic origins of the behavior.

Hwang[6] was among the first to attempt to model ferroelectric response at the microscale. In that work, the material structure is modeled explicitly as a mixture of randomly oriented *single-domain* grains, and an energy criterion is used to govern domain switching in response to external loading. The polycrystalline behavior is the average of contributions from each crystal. This approach yields qualitative agreement with observed electromechanical hysteresis phenomena. However, this model assumes single domain grains and neglects interactions among grains.

Huber et al.[7] made use of the similarity between domain switching in polydomain ferroelectric single crystals and activation of slip systems in ductile metals. The methods of crystal plasticity were employed to track the kinematics of switching systems. The model accommodates polydomain grains by using the Reuss approximation which assumes that the stress and electric field are uniform over the grain. This makes it possible to compute effective material properties from volume fractions of available domain orientations (orientation bins, or just bins) without knowledge of the actual domain configuration. The volume fractions are allowed to evolve based on an energy criterion similar to the one used by Hwang.[6] Huber's model predicts the response of a polydomain crystal but does not directly incorporate the polycrystalline character of ferroceramics.

Kamlah[8] applied a modification of Huber's model in a vector potential finite element formulation[9] to perform 2D simulations that directly resolve the polycrystal in the computational grid. Each element in the 10 by 10 grid is considered to be a single polydomain crystal with a random material basis. While this work did not provide a comparison to experimental data, the model produced expected single crystal and polycrystal results and provided insight into the behavior of a polycrystalline ferroceramic during poling.

These models, among many others, have provided the ability to analyze complex electromechanical devices and develop a more in depth understanding of ferroceramics. However, work continues in the pursuit of a predictive modeling capability and a fundamental physical understanding of these materials. The objective of this work was to simulate hydrostatic depoling of a polycrystalline ferroceramic sample. The approach used here is to resolve the microstructure directly in the topology of the problem domain and use the extended finite element method (X-FEM) to solve the governing equations of electromechanics. Each grain in the polycrystal is modeled as a single crystal with its own unique and randomly determined material basis. A micro-electromechanical material model is used that is similar to the one proposed by Huber[7] and used by Kamlah.[8] While the method can be generally applied to domain switching and phase transitions in any material, the method is used to examine mechanical depoling in PZT 95/5-2Nb.

In section 2, the extended finite element method is described and the application of X-FEM to the electromechanics problem is presented. In section 3, the single crystal material model that is used in the analysis is described. In section 4, mechanical depoling is examined under hydrostatic loading. Finally, in section 5, the conclusions of this work are summarized.

2. THE EXTENDED FINITE ELEMENT METHOD FOR ELECTROMECHANICS

The extended finite element method (X-FEM) greatly simplifies the treatment of complex geometries by incorporating material interfaces directly in the FEM interpolation.[10] In classical finite elements, geometric features are resolved in a conformal discretization. That is, the mesh must conform to external surfaces and internal interfaces. In many cases, such as with composite structures and multiple phase materials, it is a formidable task to create a conformal discretization.

X-FEM is an extension of classical FEM to treat functions with arbitrary discontinuities and discontinuous derivatives. The interface between materials is captured through a nodal enrichment function that, in this work, is based on a signed distance function.

Following Ghandi and Hagood,[11] the governing equations for the coupled electromechanical system, in both the strong and weak forms, is presented here. Consider a domain $\Omega \subset \Re^3$ with boundary $\Gamma = \Gamma_u \cup \Gamma_t = \Gamma_\phi \cup \Gamma_q$. The goal is to satisfy the conditions of mechanical and electrical equilibrium in the absence of free charge

$$\begin{array}{llll} \nabla \cdot \sigma = 0 & in\ \Omega & \nabla \cdot \mathbf{D} = 0 & in\ \Omega \\ \mathbf{u} = \mathbf{u}^{\Gamma_u} & on\ \Gamma_u & \phi = \phi^{\Gamma_\phi} & on\ \Gamma_\phi \\ \sigma \cdot \mathbf{n} = \mathbf{t}^{\Gamma_t} & on\ \Gamma_t & \mathbf{D} \cdot \mathbf{n} = -q^{\Gamma_q} & on\ \Gamma_q \end{array} \tag{1}$$

where σ is the stress, $\mathbf{D}$ is the electric displacement, $\mathbf{u}^{\Gamma_u}$ and ϕ^{Γ_ϕ} are the prescribed displacement and electric potential, $\mathbf{t}^{\Gamma_t}$ and q^{Γ_q} are the prescribed traction and charge, and $\mathbf{n}$ is the unit normal. The prescribed boundary conditions are some function of an independent load parameter, say γ, so that loads can be applied incrementally. The strain, ϵ, and electric field, $\mathbf{E}$, are expressed in terms of the independent quantities, displacement and potential, according to

$$\epsilon = \nabla_s \mathbf{u} = \frac{1}{2}\left(\nabla \mathbf{u} + \mathbf{u} \nabla\right) \tag{2}$$

$$\mathbf{E} = -\nabla \phi. \tag{3}$$

The principle of virtual work can be expressed in the preceeding terms for the mechanical part as[12]

$$\int_\Omega \sigma \delta \epsilon d\Omega = \int_{\Gamma_t} t^{\Gamma_t} \delta \mathbf{u} d\Gamma \tag{4}$$

and by observation of the similarity between the mechanical and electrical governing equations, the electrical analog to equation 4 is

$$\int_\Omega \mathbf{D} \delta \mathbf{E} d\Omega = \int_{\Gamma_q} q^{\Gamma_q} \delta \phi d\Gamma\ . \tag{5}$$

A stress field and electric displacement field satisfy the conditions of mechanical and electrical equilibrium if equations 4 and 5 are satisfied for arbitrary virtual quantities, $\delta \mathbf{u}$ and $\delta \phi$.

The discrete system of equations is achieved by the approximations

$$\begin{array}{l} \mathbf{u}(\mathbf{x}) = \sum_I \mathbf{u}_I N_I(\mathbf{x}) + \sum_J \mathbf{a}_J N_J(\mathbf{x}) \eta(\mathbf{x}) \\ \phi(\mathbf{x}) = \sum_I \phi_I N_I(\mathbf{x}) + \sum_J \rho_J N_J(\mathbf{x}) \eta(\mathbf{x}) \end{array} \tag{6}$$

where $N_I(\mathbf{x})$ are the finite element shape functions, and $\mathbf{u}_I$ and ϕ_I are the nodal displacements and potential.[10] The first term on the right hand side of equation 6 is the familiar finite element interpolation used in many conventional finite element codes. The second term is due to the extended finite element method and accounts for the C^0 continuity of an element that is bisected by a material interface. In this term, $\mathbf{a}_J$ and ρ_J are the *enrichment* degrees of freedom and exist only at those nodes whose support is intersected by a material interface. The scalar valued function, $\eta(\mathbf{x})$, is referred to as the *enrichment function*. The enrichment function selected for this work was proposed by Moes[13] and is defined to be

$$\eta(\mathbf{x}) = \sum_I |\psi_I| N_I(\mathbf{x}) - \left| \sum_I \psi_I N_I(\mathbf{x}) \right| \tag{7}$$

where ψ_I are the nodal values of the level set representation of the material boundary. The key feature of this function, illustrated schematically in figure 1, is that the first derivative is discontinuous. It is this attribute that makes the enriched interpolation of equation 6 well suited for elements with discontinuous material properties.

In this formulation the discretization takes the form of a structured cartesian grid and the geometry of the problem is captured by nodal level set values (figure 1). The task is no longer to create a discretization that conforms to the geometry but to compute the corresponding level set values, a problem that will in general be much easier.

Recasting the interpolation in equation 6 defines the interpolation matrices, $\mathbf{N_u}$ and $\mathbf{N}_\phi$ such that

$$\mathbf{u} = \mathbf{N_u U} \tag{8}$$

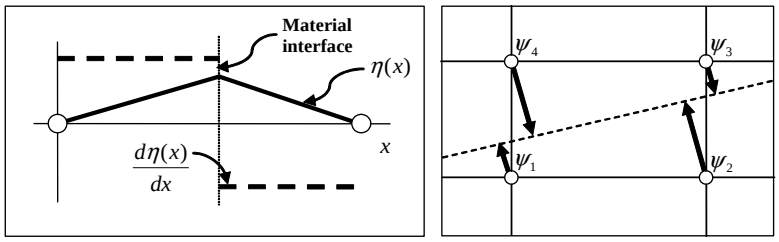

Figure 1. Schematic representation of the enrichment function.

$$\phi = \mathbf{N}_\phi \Phi \tag{9}$$

where $\mathbf{U}$ and Φ are all nodal displacement and nodal potential degrees of freedom, including enrichment. Applying the definition of strain and electric field, equations 2 and 3, to the interpolation in equations 6 yields the gradient matrices, $\mathbf{B_u}$ and $\mathbf{B}_\phi$ such that

$$\epsilon = \mathbf{B_u U} \tag{10}$$

$$\mathbf{E} = -\mathbf{B}_\phi \Phi \ . \tag{11}$$

Equations 8 through 11 are substituted into the weak form of the governing equations, equations 4 and 5, to yield

$$\delta \mathbf{U} \int_\Omega \mathbf{B_u}^T \sigma d\Omega = \delta \mathbf{U} \int_{\Gamma_t} \mathbf{N_u}^T t^{\Gamma_t} d\Gamma \tag{12}$$

$$-\delta \Phi \int_\Omega \mathbf{B}_\phi{}^T \mathbf{D} d\Omega = \delta \Phi \int_{\Gamma_q} \mathbf{N}_\phi{}^T q^{\Gamma_q} d\Gamma \tag{13}$$

where the nodal virtual quantities can be taken outside the integral since they are independent of position. The nodal forces, $\mathbf{R}$, and nodal charges, $\mathbf{Q}$, will be defined so that the inner product with the virtual quantities yields the virtual work

$$\mathbf{R}^{int} = \textstyle\int_\Omega \mathbf{B_u}^T \sigma d\Omega \qquad \mathbf{R}^{ext} = \textstyle\int_{\Gamma_t} \mathbf{N_u}^T \mathbf{t}^{\Gamma_t} d\Gamma \tag{14}$$

$$\mathbf{Q}^{int} = -\textstyle\int_\Omega \mathbf{B}_\phi{}^T \mathbf{D} d\Omega \qquad \mathbf{Q}^{ext} = \textstyle\int_{\Gamma_q} \mathbf{N}_\phi{}^T \mathbf{q}^{\Gamma_q} d\Gamma \tag{15}$$

and since equations 12 and 13 must be satisfied for arbitrary $\delta\mathbf{U}$ and $\delta\Phi$ the condition for mechanical and electrical equilibrium becomes

$$\mathbf{R} = \mathbf{R}^{int} - \mathbf{R}^{ext} = 0 \tag{16}$$

$$\mathbf{Q} = \mathbf{Q}^{int} - \mathbf{Q}^{ext} = 0. \tag{17}$$

The integrals in equations 14 and 15 are evaluated over the volume of each element and then summed to arrive at the global quantities. Elements that are not intersected by a material interface are integrated using second order Gauss quadrature. However, elements that are intersected must be integrated carefully to account for the discontinuous integrand. The approach used for this work is to integrate intersected elements by breaking the element into continuous subdomains and then further dividing the subdomains into tetrahedra. Finally, integration is done over the tetrahedra using second order accurate Gauss quadrature.

To accommodate domain switching events without limiting the load step throughout the calculation, an adaptive load stepping algorithm is used. Zeroth order parameter continuation is used wherein the load step is a function of a continuation parameter, say γ, that is selected such that a specified condition is satisfied. For an electrical or mechanical load, this condition states that the maximum change in electric displacement magnitude or any normal strain component, respectively, cannot exceed a specified limit. This approach has proven very effective in resolving nonlinear behavior while limiting the total number of load steps.

In terms of generalized degrees of freedom, $\mathcal{X}$, and nodal loads, $\mathbf{F}$, the condition for static equilibrium, equations 1, can be expressed as

$$\mathbf{F} = \left\{ \begin{array}{c} \mathbf{R}(\mathcal{X}) \\ -\mathbf{Q}(\mathcal{X}) \end{array} \right\} = 0 \tag{18}$$

where $\mathcal{X} = \{\mathbf{U}\ \Phi\}^T$, and the negative sign on the nodal charges is introduced so that the resulting stiffness matrix is symmetric.[11] The nonlinear system is solved using Newton-Raphson iteration:

$$\mathbf{K}\Delta\mathcal{X} = -\mathbf{F}(\gamma_t, \mathcal{X}_i) \tag{19}$$

$$\mathcal{X}_{i+1} = \mathcal{X}_i + \Delta\mathcal{X} \tag{20}$$

where the subscript i indicates the current iteration and γ_t is the current value of the load parameter. The stiffness matrix, $\mathbf{K}$, is computed using material finite differencing, followed by an assembly operation. Iteration continues until a convergence criterion is met then the load parameter, γ_t, is incremented and the nonlinear iteration begins anew. This process continues until the load parameter reaches a predetermined value.

3. CONSTITUTIVE MODEL

The finite element method described in section 2 is independent of the particular material being studied. The behavior of the material under consideration must be incorporated with a constitutive model that captures the salient features of the material response in the expected range of operation. If a ferroelectric ceramic is subjected to sufficiently large loads, electrical and/or mechanical, the response of the material becomes nonlinear due to the reorientation of electric dipoles and/or phase transitions. The nonlinearity of the material response is accomodated by decomposing the strain and electric displacement into their elastic (linear) and inelastic (nonlinear) parts;

$$\begin{array}{l} \sigma_i = c_{ij}^D \epsilon_j^L - h_{ij} D_j^L \\ E_i = -h_{ij} \epsilon_j^L + \beta_{ij}^\epsilon D_j^L \end{array} \tag{21}$$

where

$$\begin{array}{l} \epsilon_i = \epsilon_i^L + \epsilon_i^R \\ D_i = D_i^L + D_i^R \end{array} , \tag{22}$$

and the inelastic quantities, ϵ_i^R and D_i^R, are a function of the load history. In this paper, the term *inelastic* includes remanent quantities associated with domain switching and quantities associated with phase transitions. Evolution of inelastic strain and inelastic polarization with the applied loads is provided by the nonlinear constitutive model and should implicitly capture the evolution of the underlying domain structure of the polycrystal.

When the stored energy, w, at a material point exceeds a critical energy level, w_c, transition systems become active in order to reduce the internal energy. In the case of ferroelectric switching, domain walls move in order to realign electric dipoles with the applied field and decrease the stored electrical energy. A ferroelectric to anti-ferroelectric phase transition brought about by an applied stress is associated with a decrease in specific volume which decreases the stored mechanical energy.

The evolution of the volume fractions of the polarization and/or phase variants is computed by requiring the dissipatable energy to be less than or equal to zero,

$$\Pi = w - w_c \leq 0 \tag{23}$$

The dissipatable energy is approximated by a Taylor series in the switching systems, η^α, out to the quadratic term:

$$\Delta\Pi = \left.\frac{\partial \Pi}{\partial \eta^\alpha}\right|_{\eta_i} \Delta\eta^\alpha + \frac{1}{2} \left.\frac{\partial^2 \Pi}{\partial \eta^\alpha \partial \eta^\beta}\right|_{\eta_i} \Delta\eta^\alpha \Delta\eta^\beta. \tag{24}$$

The minimum occurs when the first derivative of Π is zero,

$$\frac{\partial \Pi}{\partial \eta^\alpha} = \left.\frac{\partial w}{\partial \eta^\alpha}\right|_{\eta_i} - \left.\frac{\partial w_c}{\partial \eta^\alpha}\right|_{\eta_i} + \left.\frac{\partial^2 w}{\partial \eta^\alpha \partial \eta^\beta}\right|_{\eta_i} \Delta\eta^\beta = 0. \tag{25}$$

Solving for the increment of $\Delta\eta^\beta$ yields

$$\Delta\eta^\beta = -\left(\mathbf{H}^{-1}\right)^{\alpha\beta}\left(\mathbf{G}^\alpha - \mathbf{G}_c^\alpha\right) \tag{26}$$

where

$$\mathbf{H}^{\alpha\beta} = \frac{\partial^2 w}{\partial\eta^\alpha \partial\eta^\beta}\Big|_{\eta_i}, \quad \mathbf{G}^\alpha = \frac{\partial w}{\partial\eta^\alpha}\Big|_{\eta_i}, \quad \mathbf{G}_c^\alpha = \frac{\partial w_c}{\partial\eta^\alpha}\Big|_{\eta_i}, \tag{27}$$

and it has been assumed that the second derivative of w_c is zero. Equation 26 amounts to a Newton-Raphson scheme when used iteratively according to

$$\eta_{i+1}^\alpha = \eta_i^\alpha + \Delta\eta^\alpha \tag{28}$$

where the subscript on η^α is the iteration index and α includes only those systems for which $G - G_c < 0$. Computing η^α in this manner requires the calculation and inversion of $\mathbf{H}$. Alternatively, a steepest descent method can be used to approximately satisfy the equilibrium condition of equation 25 wherein the increment of η^α is computed by

$$\Delta\eta^\alpha = -\tau\left(\mathbf{G}^\alpha - \mathbf{G}_c^\alpha\right). \tag{29}$$

The scaling parameter is given as $\tau = \left(\sum_n \mathbf{H}^{nn}\right)^{-1}$, where n includes only active systems. Equation 29 represents a significant reduction in computational cost *per iteration* since there is no matrix inversion and it is necessary to compute only the diagonals of $\mathbf{H}$.

3.1. Effective Crystal Properties

If the material basis is $\mathbf{R_m}$ and the crystal basis with respect to the material basis is $\mathbf{R_i}$, the rotation matrix from crystal variant I to the global frame of reference is $\mathbf{R} = \mathbf{R_m}\ \mathbf{R_i}$. Consequently, the fourth order stiffness tensor, for example, is given in the global frame by

$$C_{ijkl}^I = R_{iq}R_{jr}R_{ks}R_{lt}C_{qrst}^{Ic}$$

where C_{qrst}^{Ic} is the stiffness tensor in the crystallographic basis. The effective material constants at a material point are computed from the present values of the volume fractions, $C_{ijkl} = c^I C_{ijkl}^I$, where c^I is the volume fraction of variant I.

3.2. Kinematics

If there are n possible crystal variants, each variant can transition to every other variant, giving a possible n^2 transition systems. Using the approach of Huber,[7] the rate of change in volume fractions, $\dot{c}^I$, is related to the transition rate, $\dot{\eta}$, of active systems by a connectivity matrix,

$$\dot{c}^I = A^{I\alpha}\dot{\eta}^\alpha \tag{30}$$

where the summation on α is implied and ranges from 1 to the number of transition systems, n^2. The numbering of the transition systems proceeds sequentially through the possible transitions from variant N to variant M for $M = 1\ldots n, N = 1\ldots n$. The connectivity matrix, A, is $n \times n^2$, wherein $A^{I\alpha} = 1$ if activation of system α increases c^I, $A^{I\alpha} = -1$ if activation of system α decreases c^I, and $A^{I\alpha} = 0$ if activation of system α has no effect on c^I. The change in inelastic strain and electric displacement is computed according to $\dot{\epsilon}_{ij}^R = \epsilon_{ij}^{R\alpha}\dot{\eta}^\alpha$ and $\dot{D}_i^R = D_i^{R\alpha}\dot{\eta}^\alpha$ where $\epsilon_{ij}^{R\alpha}$ and $D_i^{R\alpha}$ are the change in inelastic strain and electric displacement associated with transition system α.

3.3. Combined Switching and Phase Transformation

In the case of combined electrical and mechanical loading, the stored energy and critical energy are expressed as

$$w = \frac{1}{2}\sigma_{ij}\left(\epsilon_{ij} - \epsilon_{ij}^R\right) + \frac{1}{2}E_i\left(D_i - D_i^R\right) \tag{31}$$

$$w_c = \frac{1}{2}\sigma_{ij}^c\left(\epsilon_{ij}^c - \epsilon_{ij}^R\right) + \frac{1}{2}E_i^c\left(D_i^c - D_i^R\right) \tag{32}$$

where a subscript or superscript 'c' indicates a critical value. Equation 31 is combined with equation 21 to yield

$$w = \frac{1}{2}\mathcal{U}\mathcal{K}\mathcal{U}^T \tag{33}$$

in terms of the material compliances,

$$\mathcal{K} = \begin{bmatrix} C_{ijkl} & -h_{ijk} \\ -h_{ijk} & \beta_{ij} \end{bmatrix}, \tag{34}$$

and independent material quantities,

$$\mathcal{U} = \begin{bmatrix} \epsilon_{ij}^L & D_i^L \end{bmatrix}. \tag{35}$$

Differentiating with respect to the transition systems, η^α, yields

$$\mathbf{G} = \frac{1}{2}\,\mathcal{U}\mathcal{K}'\mathcal{U}^T + \mathcal{U}'\mathcal{K}\mathcal{U}^T \tag{36}$$

$$\mathbf{H} = \mathcal{U}'\mathcal{K}\mathcal{U}'^T + 2\,\mathcal{U}'\mathcal{K}'\mathcal{U}^T \tag{37}$$

where the first derivatives are

$$\mathcal{U}' = \begin{bmatrix} -\epsilon_{ij}^{R\alpha} & -D_i^{R\alpha} \end{bmatrix} \tag{38}$$

and

$$\mathcal{K}' = \begin{bmatrix} C_{ijkl}^I A^{I\alpha} & -h_{ijk}^I A^{I\alpha} \\ -h_{ikl}^I A^{I\alpha} & \beta_{ik}^I A^{I\alpha} \end{bmatrix}. \tag{39}$$

The preceding steps are repeated for equation 32 to arrive at an expression for the critical transition energy. The first term on the right side of equation 36 can be neglected and the second term can be expressed in terms of a critical stress and electric field, σ_{ij}^c and E_i^c, so that the critical energy level required for activation of each transition system is given by

$$\mathbf{G}_c^\alpha = -\sigma_{ij}^c \epsilon_{ij}^{R\alpha} - E_i^c D_i^{R\alpha}. \tag{40}$$

Once η^α are computed using equations 27 through 29, the updated values of the bin fractions, c^I, inelastic strain, ϵ_{ij}^R, and inelastic polarization, D_i^R, are computed.

To model the domain switching and phase transition behavior of PZT 95/5-2Nb, all of the possible variants must be accounted for. In specific, there are 8 ferroelectric variants, one for each body diagonal of the rhombohedral unit cell, 12 anti-ferroelectric variants, one for each face diagonal of the orthorhombic unit cell, and 1 for the cubic paraelectric phase for a total of 21 variants and 441 possible transition systems. However, for the sake of efficiency, anti-ferroelectric variants with the same direction but opposite sense are treated as one. This simplification neglects anti-ferroelectric switching but reduces the total number of variants to 15 and the possible transition systems to 225. In addition, anti-ferroelectric variants that occupy the same cell face are combined to reduce the number of variants and transition systems to 12 and 144, respectively. This is possible because the orthorhombic lattice constants, a and c, of PZT 95/5-2Nb very nearly satisfy an additional constraint that $c = 2a$.

The transition strains and transition polarizations are computed as the respective differences in spontaneous strain and spontaneous polarization. When a transition occurs from FE to AFE the material point goes from a polar to anti-polar state and the transition polarization is, for a transition from FE variant [111] to AFE variant [011] ($\alpha = 9$) for example,

$$\begin{aligned} \mathbf{D}^{R9} &= \mathbf{P}^{[011]} - \mathbf{P}^{[111]} \\ \mathbf{P}^{[111]} &= P_{FE}^s \left\{ \begin{array}{ccc} 1/\sqrt{3} & 1/\sqrt{3} & 1/\sqrt{3} \end{array} \right\} \\ \mathbf{P}^{[011]} &= \left\{ \begin{array}{ccc} 0 & 0 & 0 \end{array} \right\} \end{aligned} \tag{41}$$

The transition strain for the same system is

$$\mathbf{x}^{R9} = \mathbf{x}^{[011]} - \mathbf{x}^{[111]} \tag{42}$$

Table 1. Rhombohedral material constants for PZT 95/5-2Nb.[14–16]

Rhombohedral Constants	
Elastic stiffness, c_{11}	$1.491 \times 10^{11}\ Pa$
c_{12}	$7.109 \times 10^{10}\ Pa$
c_{13}	$5.347 \times 10^{10}\ Pa$
c_{33}	$1.107 \times 10^{11}\ Pa$
c_{44}	$2.642 \times 10^{10}\ Pa$
Relative permittivity, ϵ_{11}	145.0
ϵ_{33}	335.0
Piezoelectric constant, h_{33}	$3.91 \times 10^{8} N/C$
h_{31}	$1.32 \times 10^{8} N/C$
h_{24}	$1.41 \times 10^{8} N/C$
Lattice parameter, a	4.148 Å
Lattice parameter, α	1.566
Spontaneous polarization	$0.37\ C/m^2$

Table 2. Orthorhombic material constants for PZT 95/5-2Nb.[15,17]

Orthorhombic Constants	
Elastic stiffness, c_{11}	$1.894 \times 10^{11}\ Pa$
c_{12}	$9.033 \times 10^{10}\ Pa$
c_{13}	$6.794 \times 10^{10}\ Pa$
c_{33}	$1.407 \times 10^{11}\ Pa$
c_{44}	$3.357 \times 10^{10}\ Pa$
c_{66}	$3.357 \times 10^{10}\ Pa$
Relative permittivity, ϵ_{11}	3500
ϵ_{33}	3275
Piezoelectric constant, h_{33}	$3.91 \times 10^{8} N/C$
h_{31}	$1.32 \times 10^{8} N/C$
h_{24}	$1.41 \times 10^{8} N/C$
Lattice parameter, b	4.147 Å
Lattice parameter, c	4.10 Å
Spontaneous polarization	$0.45\ C/m^2$

where the spontaneous strains are

$$\mathbf{x}^{[111]} = \begin{bmatrix} 0 & \frac{1}{2}\cos\alpha & \frac{1}{2}\cos\alpha \\ \frac{1}{2}\cos\alpha & 0 & \frac{1}{2}\cos\alpha \\ \frac{1}{2}\cos\alpha & \frac{1}{2}\cos\alpha & 0 \end{bmatrix}, \quad \mathbf{x}^{[011]} = \begin{bmatrix} \frac{1}{2}\left(\frac{b^2}{a^2}-1\right) & 0 & 0 \\ 0 & \frac{1}{2}\left(\frac{b^2}{a^2}-1\right) & 0 \\ 0 & 0 & \frac{1}{2}\left(\frac{c^2}{a^2}-1\right) \end{bmatrix}. \tag{43}$$

4. HYDROSTATIC DEPOLING

While shock-activated power supplies operate in a decidedly dynamic regime, much understanding can be provided using static material testing and modeling. Zeuch et al.[18] used static testing to examine the ferroelectric (FE) to anti-ferroelectric (AFE) phase transformation. Montgomery[19] proposed a macroscale model that predicts the hydrostatic phase transformation behavior of porous ceramics and produced good agreement with the measurements from Zeuch. In this section, hydrostatic depoling is simulated at the microscale, and results are compared with data from Zeuch.[20]

Table 3. Transition constants for PZT 95/5-2Nb.[15]

Transition Constants	
Curie temperature	228.0 C
FE to AFE transition pressure	2.53×10^8
FE coercive field	$9.3 \times 10^5 V/m$

The non-linear material model described in section 3 was used within the X-FEM formulation described in section 2 to simulate the response of fully dense and porous polycrystalline PZT 95/5-2Nb to hydrostatic loading. A structured cartesian grid with a resolution of 10x10x10 elements was used for the calculations. Material constants are given in Tables 1 through 3. The porous sample has a single pore located at the origin and has a porosity of 1.88%. While this is an over-simplification of an actual porous PZT sample, it is sufficient to get at the nature and extent of the effect of pores on material response. The load step is selected so that the change in normal strain in a single step doesn't exceed 5×10^{-6}. The load step is further limited to fall between 1×10^4 and 1×10^5 MPa.

The polycrystalline structure is modeled using a Voronoi tesselation of a cubic problem domain. The tesselation is achieved by randomly placing a given number of points (grain centers) and then allowing the points to diffuse to roughly equidistant locations based on simple interaction rules. In the porous case, the points interact with the surface of the pore so that the points are evenly distributed in the solid region. The net result is a Voronoi tesselation with grains of roughly equal size. Each grain center is then assigned a random material basis that will be the basis for anisotropic material constants. The integration points in the finite element formulation are then assigned the correct material basis according to proximity. Grain boundaries are not modeled exactly using X-FEM interfaces but are captured approximately by the classic finite element polynomial basis. This is to avoid nonessential complexity in an already expensive calculation. When voids are present in the problem domain, X-FEM is used to capture the stronger discontinuity of a free surface. One octant of the porous sample is modeled to avoid free surface interactions while minimizing the number of required elements. The same boundary conditions are applied to both configurations for the sake of uniformity.

The displacive phase transformation from ferroelectric (FE) rhombohedral to anti-ferroelectric (AFE) orthorhombic produces a compressive volumetric strain.[20] When a sample of PZT 95/5-2Nb is hydrostatically loaded to the transformation pressure, a pronounced decrease in volume occurs. Once the material is fully transformed, linear elastic response resumes in the AFE phase. Figure 2 shows the computed hydrostatic response for poled and unpoled samples. As expected, the material undergoes a substantial decrease in volume around the hydrostatic transformation pressure. Based on the lattice constants used for these calculations, the change in volume of solid PZT 95/5-2Nb should be a decrease of approximately 1.17%, which is observed in the results.

PZT 95/5-2Nb shows a gradual onset of transformation from FE to AFE, and the range of pressure over which the transformation takes place increases with the porosity of the sample.[20] Further, the onset of transformation begins at a lower pressure as porosity increases. These effects are illustrated in figure 3 which shows the measured pressure-volume response of PZT 95/5-2Nb with 4% and 10% porosity. The sample with 4% porosity exhibits a relatively sharp transition and begins to transform at a higher pressure level. Such behavior is predicted by the numerical results as shown in figure 2.

The porous samples (i.e., poled and unpoled) show similar behavior to the solid samples in that the poled case has a more gradual onset of the phase transformation than does the unpoled case. However, an important distinction is that the porous samples transform over a wider range of pressure. That is, the slope of the pressure-volume response during transformation, which is essentially zero for the solid cases, is non-zero for the porous cases. The pore introduces a larger degree of non-uniformity to the stress state which yields greater spatial variation in the phase transition.

Typically, when PZT 95/5-2Nb is unloaded, the material exhibits a partial reverse transformation, leaving the sample in a mixed FE/AFE phase. This behavior is observed in the porous configuration shown in figure 2. The non-linear decrease in volume strain that begins when the sample is unloaded to about 50 MPa is produced by a

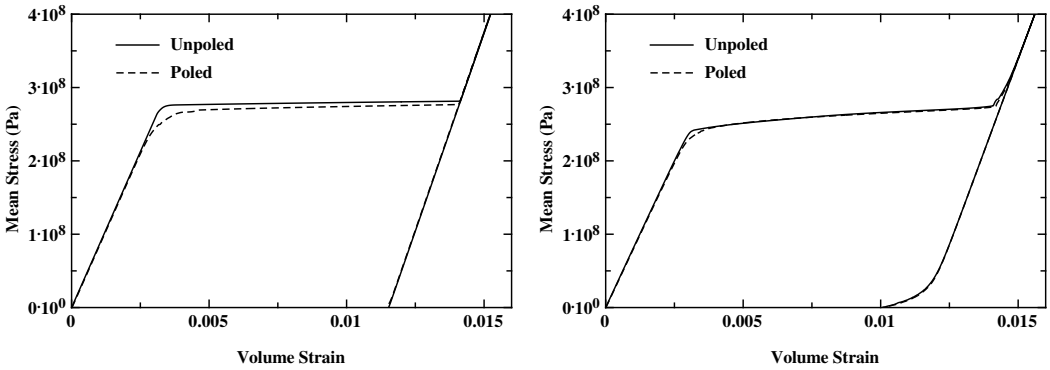

(a) Solid polycrystal (b) Porous (1.88%) polycrystal

Figure 2. Hydrostatic depoling of poled and unpoled PZT 95/5-2Nb.

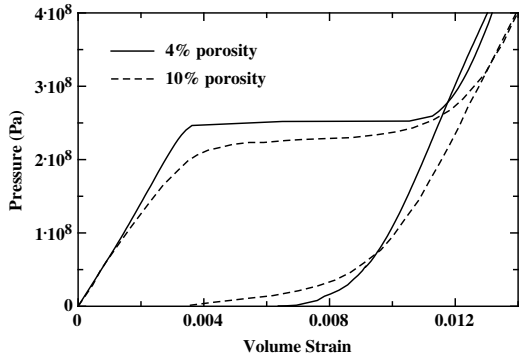

Figure 3. Measured pressure-volume response of PZT 95/5-2Nb with 4% and 10% porosity.[20]

partial reverse transformation. Since PZT 95/5-2Nb can assume a stable mixed phase, the reverse transformation from FE to AFE only occurs when the FE phase becomes unstable. The wide variation of internal stresses in the porous case provides such a condition. Figure 4 shows the stress distribution present in the simulations. The effective stress just prior to fully unloaded (at about 75 MPa applied pressure) is as high as 50 MPa for the poled solid case and 200 MPa for the porous cases.

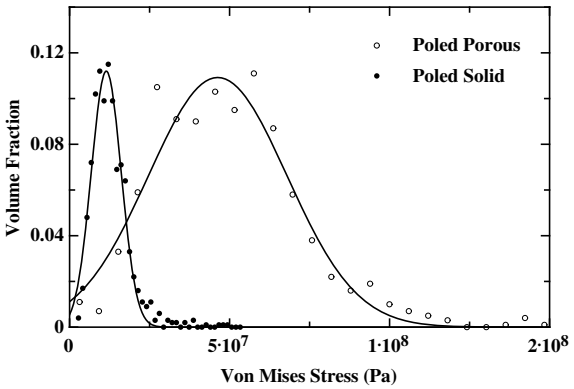

Figure 4. Distribution of internal stresses prior to complete unloading. Solid lines are Gaussian curve fits to assist the eye.

5. CONCLUSIONS

Ferroceramics represent an important class of active materials that has seen wide use in advanced and technically demanding applications. These applications require a fundamental understanding of the material response to a wide range of combined electrical and mechanical loads. Predicting material response, and optimizing such response, requires detailed knowledge of the microstructural origins of non-linear ferroelectric behavior.

The goal of this work was to develop a numerical approach that directly models microstructural features of ferroceramics and use this approach to examine the effect of these features on microscale and bulk material behavior during mechanical depoling. To that end, a microelectromechanically motivated constitutive model was used based on the methods of micromechanics. In addition to modeling the polarization variants in the ferroelectric phase, the crystal variants of the anti-ferroelectric phase were included so that simultaneous ferroelectric switching and phase transformation could be examined.

The porous configuration was treated using X-FEM so that the spherical pore was accommodated implicitly with a level set field. The grain structure, however, was approximated with the standard FEM polynomial basis. The reason for this is that accounting for multiple intersecting X-FEM surface is an ongoing area of study in the numerical methods research community. The goals of this work are nonetheless achieved using X-FEM to introduce voids in the problem domain, and treating the grain structure with the standard FEM basis.

The polycrystalline structure was approximated by a Voronoi tesselation of the domain. The limiting factor in accurate modeling of nonlinear material behavior was a unified and physically based treatment of domain switching and phase transitions, so a simplified representation of the microstructure sufficed. The methods developed for this work are not limited to this type of representation. Models of the microstructure that are physically more accurate could be used as a future refinement.

Poled and unpoled samples of solid and porous configurations were mechanically depoled with hydrostatic loading. The calculations predict that porosity produces a decrease in the pressure level at which phase transformation begins, and that the phase transformation occurs over a wider range of applied pressure. Both effects are observed in experimental measurements. Further, the calculations suggest that the reverse transformation that occurs upon unloading is driven by internal stresses, and that porosity produces higher internal stresses, and therefore a larger degree of reverse transformation, than does the polycrystalline structure. This observation is supported by measurements that show that samples with higher porosity produce a greater degree of reverse transformation.

6. ACKNOWLEDGEMENTS

We thank Stephen T. Montgomery for many helpful discussions and careful review of the manuscript. Sandia is a multiprogram laboratory operated by Sandia Corporation, a Lockheed Martin Company, for the United States Department of Energy's National Nuclear Security Administration under contract DE-AC04-94AL85000.

REFERENCES

1. B. Jaffe, W. R. Cook, and H. L. Jaffe, *Piezoelectric Ceramics*, Academic Press Limited, New York, 1971.
2. P. C. Lysne and C. M. Percival, "Electric energy generation by shock compression of ferroelectric ceramics: Normal-mode response of pzt 95/5.," *J Appl Phys* **46**, pp. 1519 – 1525, Apr 1975.
3. C. S. Lynch, "The effect of uniaxial stress on the electro-mechanical response of 8/65/35 plzt.," *Acta Materialia* **44**, pp. 4137 – 48, Oct 1996.
4. P. M. Chaplya and G. P. Carman, "Dielectric and piezoelectric response of lead zirconate-lead titanate at high electric and mechanical loads in terms of non-180 degrees domain wall motion.," *Journal of Applied Physics* **90**, pp. 5278 – 86, NOV 2001.
5. P. M. Chaplya and G. P. Carman, "Compression of piezoelectric ceramic at constant electric field: Energy absorption through non-180 degrees domain-wall motion.," *Journal of Applied Physics* **92**, pp. 1504 – 10, AUG 2002.
6. S. C. Hwang, C. S. Lynch, and R. M. McMeeking, "Ferroelectric/ferroelastic interactions and a polarization switching model.," *Acta Metallurgica et Materialia* **43**, pp. 2073 – 84, May 1995.

7. J. E. Huber, N. A. Fleck, C. M. Landis, and R. M. McMeeking, "A constitutive model for ferroelectric polycrystals.," *Journal of the Mechanics and Physics of Solids* **47**(8), pp. 1663 – 97, 1999.
8. M. Kamlah, A. C. Liskowsky, R. M. McMeeking, and H. Balke, "Finite element simulation of a polycrystalline ferroelectric based on a multidomain single crystal switching model.," *International Journal of Solids and Structures* **42**, pp. 2949 – 64, May 2005.
9. C. M. Landis, "A new finite-element formulation for electromechanical boundary value problems.," *International Journal for Numerical Methods in Engineering* **55**, pp. 613 – 28, OCT 2002.
10. T. Belytschko, C. Parimi, N. Moes, N. Sukumar, and S. Usui, "Structured extended finite element methods for solids defined by implicit surfaces.," *International Journal for Numerical Methods in Engineering* **56**, pp. 609 – 35, Jan 2003.
11. K. Ghandi and N. W. Hagood, "Nonlinear finite element modeling of phase transitions in electromechanically coupled material.," *Proceedings of the SPIE - The International Society for Optical Engineering* **2715**, pp. 121 – 40, 1996.
12. L. Malvern, *Introduction to the Mechanics of a Continuous Medium*, Prentice-Hall, Inc., New Jersey, 1969.
13. N. Moes, M. Cloirec, P. Cartraud, and J. F. Remacle, "A computational approach to handle complex microstructure geometries.," *Computer Methods in Applied Mechanics and Engineering* **192**, pp. 3163 – 77, Jul 2003.
14. K. Leung, "Progress on ab initio calculations of PZT properties," tech. rep., Sandia National Laboratories, 2000.
15. M. Y. Lee, S. T. Montgomery, J. H. Hofer, and D. H. Zeuch, "Hydrostatic, uniaxial, and triaxial compression tests on unpoled "chem-prep" PZT 95/5-2nb ceramic within temperature range of -55 to 75^o c," Tech. Rep. SAND2003-3651, Sandia National Laboratories, 2003.
16. W. Drotning and D. Kirby, "Thermal expansion of ferroelectric ceramics," tech. rep., Sandia National Laboratories, 1984.
17. B. A. Tuttle, J. A. Voigt, T. W. Scofield, P. Yang, D. H. Zeuch, and M. A. Rodriguez, "Dielectric properties and depoling characteristics of $Pb(Zr_{0.95}Ti_{0.05})O_3$ based ceramics: Near-critical grain size behavior," Tech. Rep. SAND99-2556, Sandia National Laboratories, 1999.
18. D. H. Zeuch, S. T. Montgomery, and J. D. Keck, "Hydrostatic and triaxial compression experiments on unpoled pzt 95/5-2nb ceramic: the effects of shear stress on the F_{R1} to A_o polymorphic phase transformation.," *Journal of Materials Research* **7**, pp. 3314 – 32, Dec 1992.
19. S. T. Montgomery and D. H. Zeuch, "A model for the bulk mechanical response of porous ceramics exhibiting a ferroelectric-to-antiferroelectric phase transition during hydrostatic compression.," *Ceramic Engineering and Science Proceedings* **25**(4), pp. 313 – 18, 2004.
20. D. H. Zeuch, S. T. Montgomery, J. D. Keck, and D. J. Zimmerer, "Hydrostatic and triaxial compression experiments on unpoled PZT 95/5-2Nb ceramic: The effects of shear stress on the $F_{R1} - A_o$ polymorphic phase transition," Tech. Rep. SAND92-0484, Sandia National Laboratories, 1992.